ACS PHYSICAL CHEMISTRY Au
AN OPEN ACCESS JOURNAL OF THE AMERICAN CHEMICAL SOCIETY

pubs.acs.org/physchemau
Article

Long-Range Conductivity in Proteins Mediated by Aromatic Residues

Siddharth Krishnan, Aleksei Aksimentiev,* Stuart Lindsay,* and Dmitry Matyushov*

Cite This: ACS Phys. Chem Au 2023, 3, 444–455
Read Online

ACCESS | Metrics & More | Article Recommendations | Supporting Information

ABSTRACT: Single-molecule measurements show that many proteins, lacking any redox cofactors, nonetheless exhibit electrical conductance on the order of a nanosiemen over 10 nm distances, implying that electrons can transit an entire protein in less than a nanosecond when subject to a potential difference of less than 1 V. This is puzzling because, for fast transport (i.e., a free energy barrier of zero), the hopping rate is determined by the reorganization energy of approximately 0.8 eV, and this sets the time scale of a single hop to at least 1 μs. Furthermore, the Fermi energies of typical metal electrodes are far removed from the energies required for sequential oxidation and reduction of the aromatic residues of the protein, which should further reduce the hopping current. Here, we combine all-atom molecular dynamics (MD) simulations of non-redox-active proteins (consensus tetratricopeptide repeats) with an electron transfer theory to demonstrate a molecular mechanism that can account for the unexpectedly fast electron transport. According to our MD simulations, the reorganization energy produced by the energy shift on charging (the Stokes shift) is close to the conventional value of 0.8 eV. However, the non-ergodic sampling of molecular configurations by the protein results in reaction-reorganization energies, extracted directly from the distribution of the electrostatic energy fluctuations, that are only ∼0.2 eV, which is small enough to enable long-range conductivity, without invoking quantum coherent transport. Using the MD values of the reorganization energies, we calculate a current decay with distance that is in agreement with experiment.

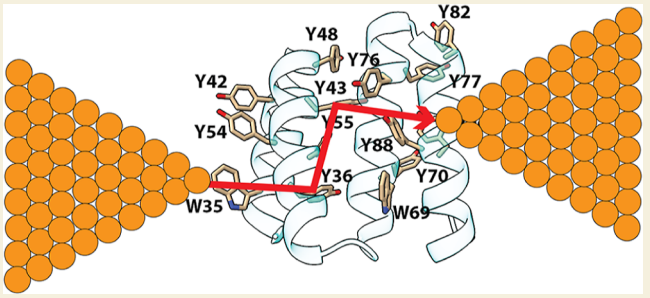

KEYWORDS: *electron transport, molecular dynamics, single-molecule conductance, reorganization energy, molecular electronics, break junctions*

INTRODUCTION

Proteins participating in the energy chains of biology (photosynthesis and respiration[1] and other enzymatic reactions) have to change the oxidation state of their active sites. Since amino acids are mostly redox-inactive, the prevailing dogma in the field is that changes in the oxidation state are achieved by utilizing redox-active cofactors intercalated into the protein fold. However, proteins that do not contain any redox cofactors are quite conductive,[2,3] challenging the view that the amino acids are redox-inactive. This possibility has been considered in studies of electron relays in proteins[4−8] where protein residues effectively act as semiconductor elements to facilitate the exchange of electrons between active sites. This conductivity mechanism adds versatility to redox-active enzymes because direct tunneling in biology is limited to ∼1.4 nm.[9] If protein residues conduct, can they do so on the time scales of an enzymatic turnover and can the observed long electronic decay lengths be accounted for?

It is often suggested that the barrier required for the electron to reach the tunneling configuration to hop between the localization sites is described by Marcus theory[10] with a "universal" protein reorganization energy[9] λ of ∼ 0.8 eV and a reaction free energy ΔG. The latter should be close to zero for hops between equal residues, in which case the barrier is mostly determined by the magnitude of λ. Some dependence of the tunneling probability on the bridging medium was found,[11] but the experimental distinctions between intervening media are not yet sufficient to allow for selection of specific tunneling pathways through particular amino acid residues. These two components, a fairly large and uniform reorganization energy, and the lack of knowledge of a specific tunneling path, are obstacles for calculating the conductivity occurring via hops between aromatic residues (mostly tryptophans, tyrosines, and histidines[7,12]). In particular, the rates of individual hops are not sufficiently high to allow for a hopping conductivity of the magnitude observed experimentally.[2,3,13,14]

Received: March 30, 2023
Revised: May 18, 2023
Accepted: May 19, 2023
Published: June 2, 2023

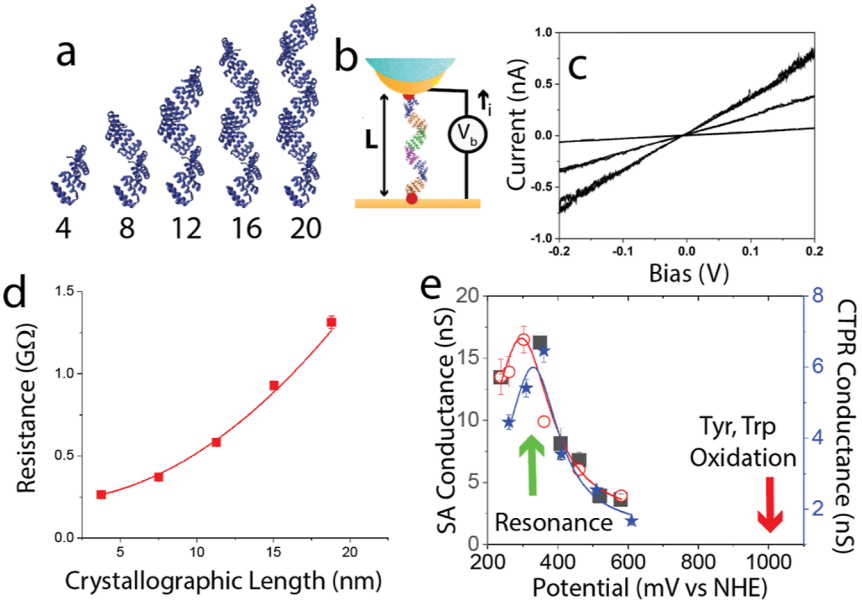

Figure 1. Experimental single-molecule conductance as a function of length of linear proteins. (a) Five CTPR proteins differing by the number of the repeat units as listed below the images. (b) Schematic of a scanning tunneling microscopy (STM) measurement of protein conductance. Cysteines (red dots) at the N- and C- termini form contacts between the protein and the metal electrodes. (c) Electrical current versus electrode voltage difference. Examples of recordings from 3 different CTPR8 molecules are shown. Many such recordings yield a distribution of single-molecule resistances. (d) Most probable resistance of a CTPR protein versus its length. The resistance does not increase linearly with L but rather as L^2 (red line) with an intercept of 0.22 GΩ. (Data from ref 3). (e) Molecular conductance depends on charge injection potential, as controlled by the Fermi energies of the metals used (black squares) or by changing surface polarization under potential control (open circles)—data (from ref 16) are for streptavidin (SA) in both cases. Stars indicate data for CTPR8, the protein considered here (data from ref 3). For both proteins, the conductance has a maximum at about 300 mV vs the normal hydrogen electrode, NHE, (green arrow), well removed from the oxidation potentials of tyrosine and tryptophan at ∼1 V vs NHE (red arrow).

The conductance of single protein molecules can be measured directly, provided that chemical contacts are utilized to inject charge,[2] and a summary of one such set of measurements[3] for a series of linear proteins (consensus tetratricopeptide repeat—CTPR—proteins) is given in Figure 1. These proteins consist of a two-helix motif that is readily concatenated via recombinant techniques to form oligomers of a controlled length. The measured single molecule resistance is ∼1 GΩ over a distance of 15 nm, fairly typical of many non-redox-active proteins.[2] This equates to a current of 0.1 nA at a bias of 0.1 V or about one electron passing from one contact to the other every ns. In contrast, an estimate (cf. eq 5) of the hopping time for a characteristic 0.6 nm distance with λ = 0.8 eV yields a time between hops of ∼1 μs, 3 orders of magnitude too slow for even a single hop. Eshel et al.[15] have pointed out that similar problems arise in an analysis of OmcS bacterial wires—specifically that in order to account for the measured conductivity, a reorganization energy of below 0.2 eV and a fast diffusion constant (∼20 nm^2/ns) are required.

A second problem lies in the electrochemical potential dependence of the conductance.[16] This is measured either by changing electrode materials (to change the Fermi energy) or by changing the surface polarization of a given metal under electrochemical potential control.[16] The conductance measured by either method shows a sharp maximum at ∼300 mV vs the normal hydrogen electrode, NHE (Figure 1e). This is quite different from the ∼1 V vs NHE required to oxidize tyrosine and tryptophan.[17,18] As we shall show, these challenges are largely resolved with the appropriate treatment of the reorganization energy.

Below, we describe the required modification to Marcus theory, then use all-atom molecular dynamics (MD) simulations to calculate the effective reorganization energy for charge transfers among the aromatic residues of CTPR monomers and dimers, and calculate the relative displacements of these residues, in order to calculate the hopping rates. A kinetic Monte Carlo simulation of the carrier diffusion, taken together with a model for charge injection, correctly accounts for the observed current decay with distance.

Modifications to Marcus Theory

Here, we use the approach of Warshel[19] who amended the Marcus picture of crossing parabolas by specifying the energy gap X between the donor and acceptor energies of the electron as the reaction coordinate. The probability of reaching the tunneling configuration, $X = 0$, is given by Gaussian statistics as a consequence of long-range electrostatics of the electron interacting with many particles in the medium (i.e., the central limit theorem). The combination of the Gaussian distribution of the reaction coordinate X with the fluctuation−dissipation theorem (FDT)[20,21] leads to a specific connection between the separation of distribution maxima in the initial and final states (the Stokes-shift reorganization energy, λ^{St}[22]) and the Gaussian width, $\sigma_X = \sqrt{2\lambda k_B T}$, specified by the Marcus reorganization energy λ. The Marcus theory utilizes this connection to establish a single reorganization energy for electron transfer $\lambda^{St} = \lambda$.

This simplification leads to the activation barrier for hopping electron transfer $\Delta G^{\dagger}$ in terms of the two parameters, the reorganization energy λ and the reaction free energy ΔG

$$\Delta G^{\dagger} = \frac{(\lambda + \Delta G)^2}{4\lambda} \quad (1)$$

https://doi.org/10.1021/acsphyschemau.3c00017
ACS Phys. Chem Au 2023, 3, 444−455

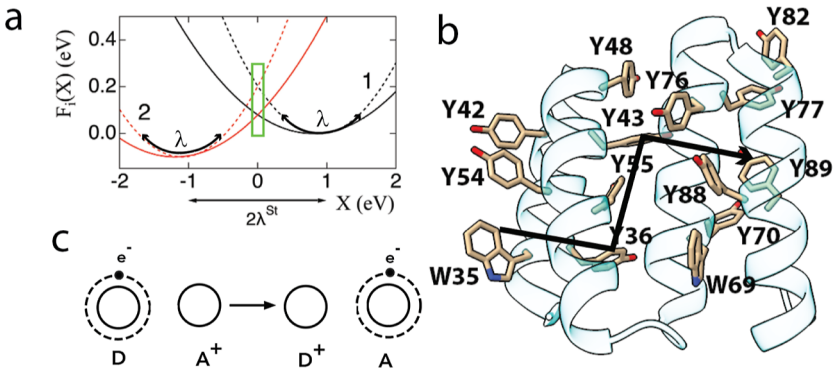

Figure 2. Hopping mechanism. (a) Schematic free energy diagram of a donor (D)−acceptor (A) pair as a function of the electrostatic potential difference X between the states before ("1") and after ("2") a charge transfer. The potential difference between the free energy minima is twice the Stokes shift for optical transitions, λ^{St}. Tunneling transitions occur where the parabolas intersect (green box). In Marcus theory, λ^{St} also determines the width of the parabolas (dashed lines) through the fluctuation−dissipation theorem. However, when electron transfer is fast compared to the thermal equilibration time, the width of the parabolas (solid lines) is no longer determined by λ^{St} and must be explicitly calculated from the distribution of energy fluctuations, leading to a reduced reorganization energy, λ^{r}, with a corresponding reduction in the barrier for electron transfer (compare the crossing point of the solid parabolas vs the crossing point of the dashed parabolas). (b) Hopping occurs via aromatic residues. Two repeat units of CTPR protein are shown with tyrosines and tryptophans highlighted (numbering includes an N-terminal tail). The arrow shows one of the many paths through the two turns of protein, with W35 as the entry point and Y89 as the exit. (c) Residues participating in the charge shift reaction change their oxidation state as illustrated (D = electron donor and A = electron acceptor).

While the Gaussian distribution of the energy gap is a general consequence of statistics of many interacting particles, the application of the FDT to the statistics of the energy gap requires a Gibbsian ensemble based on the assumption that all "essential" configurations are accessible by the protein thermal bath on the reaction time scale. This is often not the case for a solvated protein, as the thermal bath, and many configurations are not accessible, either because they require times that are too long to be reached or they are thermodynamically unstable (e.g., protein unfolding) or geometrically prohibited by closely packed folded protein. Overall, a folded protein is a frustrated (glassy[23]) medium with many dynamical and geometrical constraints imposed on the configurations coupled to the reaction coordinate. These frustrations lead to a non-Gibbsian statistics of thermal fluctuations and to violations of the FDT.[22] When sampling is incomplete (non-ergodic), the direct correspondence between λ^{St} and λ is broken. In particular, the parabolas connecting the free energy distributions to X can be broader (solid lines in Figure 2a) than predicted by Marcus theory (dashed lines in Figure 2a), leading to an effective (reaction) reorganization energy[22,24]

$$\lambda^{r} = \frac{(\lambda^{St})^2}{\lambda} \tag{2}$$

that replaces the Marcus λ in eq 1. Simulations of electron transfer between redox cofactors in electron-transfer proteins showed $\lambda^{St} < \lambda$, and thus, there is a lower barrier for hopping electron transfer than suggested in the Marcus framework.[22,24−29] Low activation barriers achieved through $\lambda^{r} < \lambda$ can potentially lead to sufficiently fast hops between aromatic residues, thus forming conductivity relays for protein electron transfer.[5,6] However, the required inequality $\lambda^{St} < \lambda$ has been established only for protein cofactors,[22,27,30,31] and it remains unclear if the inequality also applies to hopping conductivity through aromatic residues. According to our MD simulations (described below), a significant reduction of the activation barrier is indeed achieved for electron hops between tyrosine and tryptophan residues due to $\langle \lambda^{St}/\lambda \rangle \approx 0.4$. This ratio also enters the non-ergodic reaction free energy which is modified from the thermodynamic value ΔG_0 to

$$\Delta G = (\lambda^{St}/\lambda)\Delta G_0 \tag{3}$$

Taking the ratio of the reorganization energies into account, the non-equilibrium redox potential of the tyrosines and tryptophans approaches the experimentally determine value of ∼300 mV vs NHE, Figure 1e.

The next important question is how individual random hops of charge carriers combine to generate the overall current and how the protein conductivity scales with the distance between the points of charge injection connected to external electrodes. The experimental data[3] summarized in Figure 1 (and data from other experiments[14,32]) show a very slow decrease of conductivity with the size of the protein. Previous studies suggested that this weak scaling reflects coherent tunneling of electrons through the entire protein.[33,34] This proposal is controversial,[35] an issue we return to in the discussion.

Here, we propose that conductivity in proteins lacking redox cofactors can be explained by random hopping of charge carriers over the network of tyrosines and tryptophans (Figure 2b) upon injection of the charge carriers at the electrode contact sites. The conductivity of redox-inactive proteins is mostly determined by the chemistry of the contact,[2] and the externally imposed bias is dropped largely at the contacts. The random walk does not involve a significant external driving force, so the dependence of conductivity on the protein size is determined by the hopping sites involved and the hopping rates. We develop a quantitative theory using all-atom simulations to calculate the electrostatic energy fluctuations of donor and acceptor sites in the initial and final states, thus deriving the effective reorganization energies and the free energies for the various hops between multiple pairs of aromatic residues located within the Dutton radius[9] (1.4 nm). The effective reorganization energies are used to calculate the hopping rates, from which a diffusion constant is derived, via a set of Monte Carlo simulations, leading to calculation of the experimentally observed quantities.

https://doi.org/10.1021/acsphyschemau.3c00017
ACS Phys. Chem Au 2023, 3, 444−455

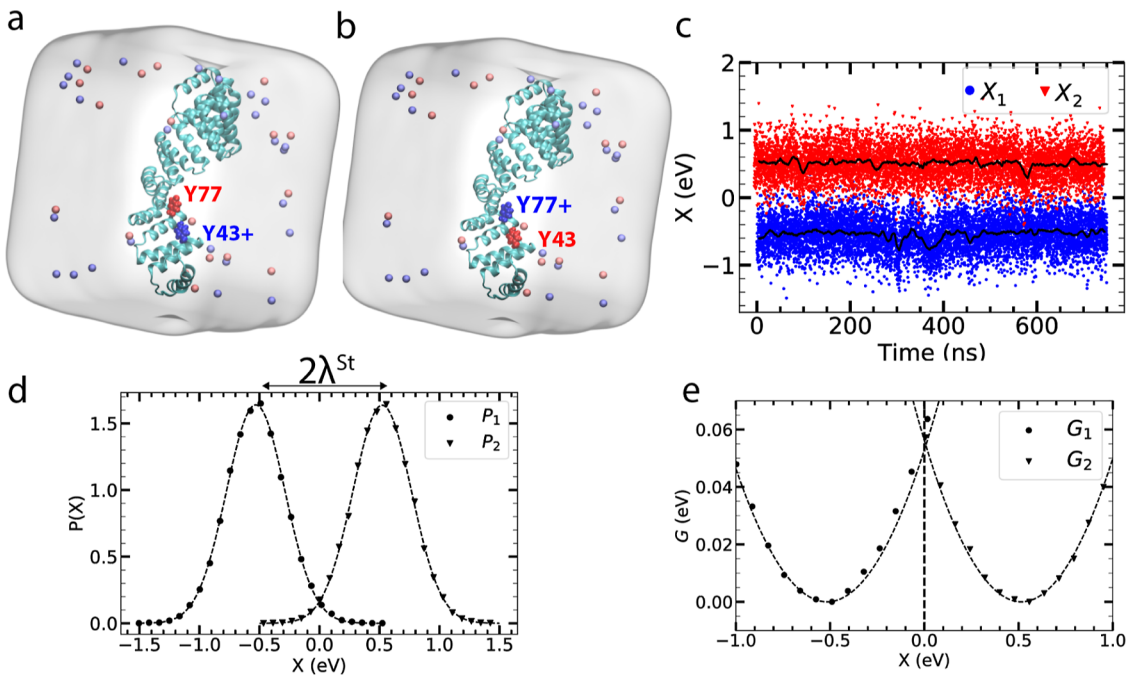

Figure 3. MD simulations of the electrostatic energy gap produced by a charge transfer process. (a) All-atom simulation system representing the initial state of the Y77-to-Y43 charge transfer process, with Y43 being positively charged (oxidized) and Y77 being electrically neutral. (b) Final state of the Y77-to-Y43 Franck−Condon charge transfer, with Y43 being neutral and Y77 being positively charged. (c) Energy gap fluctuations at Y43 (X_1) and Y77 (X_2). The black traces indicate 10 ns block average of the 10 ps sampled raw data. (d) Electrostatic energy probability distributions for the positively charged Y43 (triangles) and positively charged Y77 (circles). The separation between the distributions' peaks is $2\lambda^{St}$. (e) Free energy as a function of the donor−acceptor electrostatic energy gap: the intersection at $X = 0$ defines the transition state.

Extracting Local Hopping Rates from Molecular Dynamics Simulations

A CTPR8 protein contains a total of 60 aromatic residues, out of which 52 are tyrosines and 8 are tryptophans. The protein consists of eight two-helix repeat units with each unit containing 34 amino acids in length and containing 6 tyrosines and 1 tryptophan (two such units − excluding the N- and C- terminal sequences − are shown in Figure 2b). We hypothesized that, during the charge transfer, these residues are oxidized to their cationic free radical states (Figure 2c). We probed this possibility by conducting all-atom MD simulations of the protein having the aromatic residues in their neutral and oxidized states and using the fluctuations of the residues' electrostatic energy to compute the rate of inter-residue electron transfer. We assume that the residues remain protonated during charge transfer because deprotonation is a slower process than the sub-nanosecond charge transfer times calculated here[36,37] (although sub-nanosecond deprotonation of tryptophan has been reported for the special case of DNA photolyases,[38] deprotonation of oxidized tryptophans occurs on the time scale of ∼200 ns[39,40]). However, should deprotonation of tyrosine occur, unpublished calculations of the electron transfer rate in a mutated azurin show that rates are not affected.

Figure 3a,b illustrates two all-atom systems used to probe a transfer of an electron from residue Y77 to Y43. In the initial state of the hopping process (Figure 3a), Y43 is in its oxidized state, whereas Y77 is charge neutral. At the end of the hopping process, Y77 is oxidized and Y43 is neutral (a Franck−Condon transition not altering the nuclear positions is shown in Figure 3a,b). To evaluate the rate of electron transfer, we computed equilibrium fluctuations of the electrostatic energy gap $X(t) = \sum_i \Delta q_i \Phi_i$, where the sum runs over all atoms of the two residues accepting or donating an electron, $\Delta q_i = q_i^{\text{final}} - q_i^{\text{initial}}$ is the change of the partial charge of atom i upon transfer of the electron, and Φ_i is the local electrostatic potential at atom i. Knowing the partial charges on the oxidized forms of a tyrosine[41] and a tryptophan[42] residue (Tables S4 and S5), we determined the energy gap fluctuations by performing a 0.75 μs equilibration of each system and evaluating the instantaneous distribution of the electrostatic potential every 10 ps using the PMEpot plug-in of VMD.[43,44] Figure 3c plots the resulting $X(t)$ data for the initial and the final states of the Y77−Y43 transfer, whereas Figure 3d shows their statistical distributions (calculated by distributing the $X(t)$ values into 25 equally sized bins within the range of the function). The corresponding free-energy distributions of the Y77−Y43 pair, obtained from the electrostatic energy gap statistics as $G_i = -k_B T \ln[P_i(X)]$, are shown in Figure 3e.

Electron transfer occurs at the point of crossing of these two distributions ($X = 0$ in Figure 3e). The variance of the distribution yields λ from $\lambda = \sigma_X^2/2k_BT$. For this particular D−A pair, the full width of the X distribution is ∼0.5 eV, yielding $\sigma \sim$ 0.24 eV and $\lambda \sim$ 1.15 eV. Thus, the free-energy parabolas are wider than the Stokes shift ($\lambda^{St} \sim$ 0.52 eV Figure 3d) would predict. For this particular transfer reaction, eq 2 yields $\lambda^r = 0.24$ eV, substantially less than the value derived either from the Stokes shift or from the distribution variance.

Similar calculations (see the Methods section) were carried out for all pairs of aromatic residues within the Dutton radius (1.4 nm edge-to-edge distance, as calculated from MD trajectories) within two repeat units, which, together with the periodicity of the CTPR8 protein, encompassed all likely electron transfer paths. Test simulations carried out for equivalent pairs of residues from different protein units have

https://doi.org/10.1021/acsphyschemau.3c00017
ACS Phys. Chem Au 2023, 3, 444−455

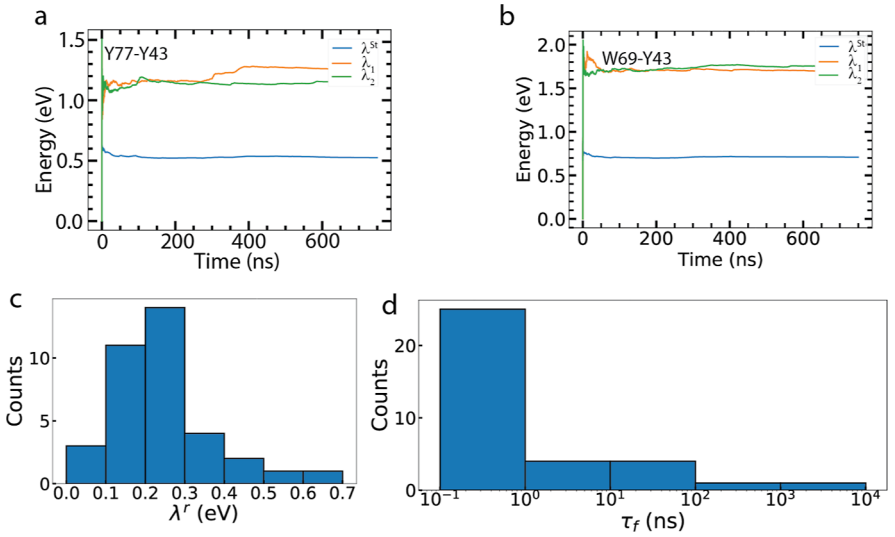

Figure 4. Calculation of reorganization energies. (a,b) Reorganization energies for a tyrosine−tyrosine (panel a) and a tyrosine−tryptophan (panel b) electron transfer calculated as $\lambda = \sigma_X^2/(2k_BT)$. The green and orange curves show cumulative average values of λ for the two charge shift reactions. The two values should be equal, in principle, and hence, their average, λ, is used in subsequent calculations. The blue curve indicates λ^{St}. As λ is substantially greater than λ^{St}, $\lambda^r=(\lambda^{St})^2/\lambda$ is substantially smaller than λ^{St}. (c) Distribution of λ^r values calculated for all pairs of aromatic residues located within the Dutton radius of each other. The modal value of the distribution is 0.2 eV, four times smaller than 0.8 eV derived from the Stokes shift. (d) Distribution of the hopping times calculated from the distributions of λ^r, the corresponding edge-to-edge donor−acceptor distances, and using the polarizability adjusted reorganization energies. The modal time is ∼100 ps, consistent with the experimentally observed nA currents.

explicitly verified the convergence of our rate calculations, Figure S1. Thus, taking the repeat structure of the protein into account, we only needed to calculate the activation energies for residue pairs within one protein unit and between the two adjacent units.

Figure 4a,b shows cumulative averages of the MD-determined reorganization energy values for a representative Y−Y and W−Y residue pair. Note here that λ_1 (orange trace) is for the D−A$^+$ state and λ_2 (green trace) is for the D$^+$−A state (defined in Figure 2c). In either configuration, λ is the solvation-free energy of the electron transfer dipole, which is "−" on the acceptor and "+" on the donor. Since the charge distribution is the same, λ is expected to be the same in both states and indeed $\lambda_1 \approx \lambda_2$. The average of the two values is used in what follows.

The distribution of λ^r values, computed according to eq 2, is plotted in Figure 4c. The modal number extracted from our simulations was 0.2 eV. A list of the values of λ^{St}, λ_{var}, ΔG, λ^r, and edge-to-edge distances for all interacting pairs within a Dutton radius is given in Table S1. As these simulations employed a non-polarizable force field, they neglected possible contributions of induced dipoles that would screen the electrostatic interactions, leading to even further reduction of the reorganization energy.[45] To account for such electronic screening, we introduced a correction factor of 0.8,[46] as discussed in detail in the Supporting Information. The correction factor was applied to both λ^{St} and λ, yielding an even lower modal value of λ^r of 0.16 eV, substantially smaller than 0.8 eV, a value commonly accepted for proteins. The activation barrier (for $\Delta G = 0$) is $\lambda^r/4$, so $\lambda^r = 0.16$ eV gives an activation barrier of 40 meV, nearly equal to the kinetic thermal energy $(3/2)kT$ at room temperature. Overall, these data yield an average value for $\langle\lambda^{St}/\lambda\rangle \approx 0.4$. Since the oxidation potential of tyrosine and tryptophan in solution includes a reorganization energy between 0.5 and 2 eV,[17,18] the reduction of reorganization energy in a protein-aqueous medium to 0.16 eV could account for the resonant injection of charge (Figure 1e and eq 3) because the potential of the (non-equilibrium) oxidized state will be shifted toward the vacuum by ∼0.7 eV. Note that we have not included intramolecular reorganization (of ∼0.2 eV[45,47,48]) because quantum intramolecular vibrations do not contribute to the activation energy in the normal regime[47] (i.e., the driving force does not exceed the reorganization energy).

Our calculation of the hopping rates proceeds as follows. The charge transfer rate k_{ET} is given by

$$k_{ET} = (1 + g(R))^{-1} k_{NA} \tag{4}$$

where the non-adiabatic transfer rate, k_{NA}, is given by

$$k_{NA} = \frac{V_{DA}^2}{\hbar}\sqrt{\frac{\pi}{k_BT\lambda^r}}\exp\left[\frac{1}{2}\gamma^2\langle(\delta R)^2\rangle - \frac{\Delta G^\dagger}{k_BT}\right] \tag{5}$$

and the activation barrier $\Delta G^\ddagger$is given by eq 1 in which λ is replaced with λ^r, the reaction free energy is from eq 3, and the equilibrium reaction free energy is zero for Y−Y pairs and −0.18 eV for Y−W pairs (Table S1). Furthermore, $\langle(\delta R)^2\rangle$ is the variance of the donor−acceptor center of mass distance. The crossover parameter $g(R)$ (see the Methods section and Supporting Information, eqs S1−S7) accounts for solvent dynamical control[49] of the rate pre-exponential factor.[50−52] The factor $g(R)$ includes two dynamic components: the Stokes shift of the energy gap $X(t)$ and the donor−acceptor distance, $R(t)$, modulating the donor−acceptor electronic coupling V_{DA}.[53] V_{DA} decays exponentially with the donor−acceptor edge-to-edge distance and is calculated here from the Hopfield equation[54]

$$V_{DA} = \frac{2.7\text{ eV}}{\sqrt{N_DN_A}}\exp\left(-\frac{\gamma}{2}R\right) \tag{6}$$

where R is the edge-to-edge distance (in nm—see Table S1) and $N_{D,A} = 7$ for a tyrosine and 9 for a tryptophan. $\gamma/2$ is the distance decay parameter, equal to 7.7 nm^{-1}.[54] This approximation has been extensively tested by Beratan and co-workers,[55,56] and a

https://doi.org/10.1021/acsphyschemau.3c00017
ACS Phys. Chem Au 2023, 3, 444−455

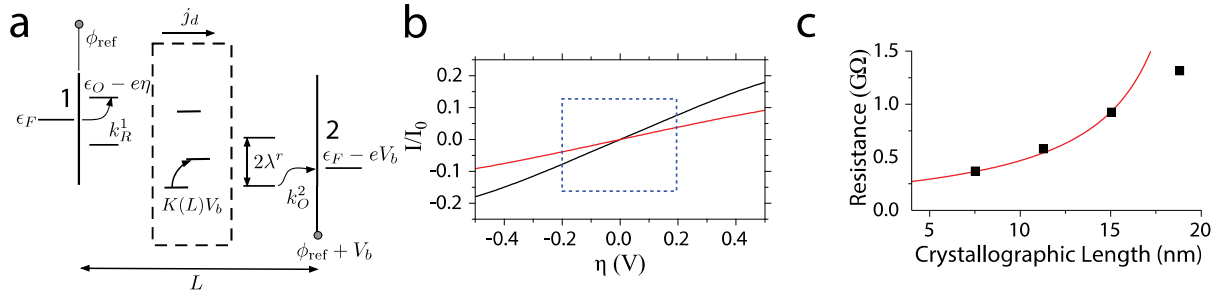

Figure 5. Charge injection model of the current. (a) Electron is extracted at the right contact 2 (energy $\epsilon_F - eV_b$) at a rate k_O^2 via the oxidation of the closest aromatic residue. The oxidized state then diffuses, through a sequence of hops, within the body of the protein (dashed box, current density j_d) to be collected by the contact 1 on the left via reduction of the closest residue at a rate k_R^1. ϵ_F is the Fermi energy of the electrodes, V_b is the applied bias, η is the potential drop at the contacts, and ϕ_{ref} is the potential of the electrodes with respect to a reference electrode. The arrows show the direction of electron motion. $K(L)$ is the experimentally determined fraction of the bias that is dropped across the bulk of the protein (Figure S2). (b) Calculated current−voltage dependences for L = 10 nm (black) and L = 15 nm (red) where the current is expressed in units of the saturation current I_0. The curves are linear in the ±200 mV range (blue box), as observed in the experiments (Figure 1c). (c) Calculated resistance vs length (red line) fit experimental data (squares) with I_0 = 5.5 nA, and the parameter a = 3.8 (see the text for details). The non-linearity arises from the combination of the distance dependence of hopping diffusional current with the length-dependent potential drop across the contacts. Fits were to conductance data, which weighted the lower resistance points.

comparison with ab initio calculations[47,56] is given in Figure S5. Taken together with the activation barriers obtained from the MD simulations, these equations yield the hopping times for all pairs within the Dutton radius in the protein, and the distribution of these times is plotted in Figure 4d, and the forward and backward rates are listed in Table S2.

Although the overall electric current is determined by the carrier velocities and not by the transit times per se, the hopping times of ∼0.1 ns (Figure 4d) are consistent with the nA currents measured in these molecules and are much smaller than 1 μs estimated for λ = 0.8 eV. The dynamical crossover parameter $g(R) \propto V_{DA}^2$ gains its distance dependence from the electronic coupling. Therefore, for $g(R) > 1$, the term V_{DA}^2 cancels in eq 4 and the rate constant becomes insensitive to the electronic coupling. Many electron hops fall in this regime of dynamical control (Table S2): for instance, charge transfer between Y77 and Y43 shown in Figure 3 produces $g \approx 28$. Because of a large number of steps with $g(R) > 1$, the overall current is not particularly sensitive to a specific model adopted for V_{DA}. The dynamical control introduces the dependence of the electron-transfer kinetics on protein dynamics and elasticity which are absent in traditional theories.

Calculation of Currents and Current Decay Rate from Hopping Rates

The current through the molecule depends on both the diffusion constant (obtained from hopping rates below) and the charge-injection rate, for which a model is also required. The decay of current with distance is described by a parameter that depends on the electronic coupling between the electrodes and the entry/exit residues, the size of those residues, and the diffusion constant, as we will show below. The electronic coupling can be estimated from the measured contact resistance and the known size of the entry/exit residues, leaving the diffusion constant to be determined.

A model of the electrode-protein system is shown in Figure 5a, from which we derive an expression for the current through the complex, below. Electrons are extracted from the residue closest to the right (positive) electrode (2 on Figure 5a) and injected in a similar way from the residue closest to the left (negative) electrode (1 in Figure 5a). The experimentally determined contact resistance (Figure 1d) is a significant fraction of the overall resistance, particularly for the shorter molecules. The fraction, $K(L)$, of the applied bias dropped across the bulk of the molecule was determined using an elementary circuit analysis,[3] and a fit to $K(L)$ is shown in Figure S2. However, even in the longest molecules, where a significant fraction of the bias is dropped across the protein, the applied field is small compared to the internal fields within the protein (see, for example, Figure 4 of Martin et al.[57]). Thus, once injected, the charges diffuse under the driving force of the carrier gradient owing to electron injection at contact 1, until captured by contact 2, a process characterized by the carrier diffusion constant.

Diffusion Constant

The diffusion constant connects the diffusion flux to the gradient of the volume density of charge carriers in the macroscopic Fick's law. A one-dimensional Brownian walker stepping the distance Δx in each step requiring time τ has the diffusion constant $D = (\Delta x)^2/(2\tau)$. The challenge of extending this equation to carrier diffusion in the protein is that both the step Δx and the hop time τ become distributed variables. The problem is solved analytically by Derrida's model[58] which sets up diffusion on a one-dimensional periodically replicated chain of sites with fixed Δx and forward and backward transition rates specified at each lattice site. This solution does not allow distributed values of Δx and provides no algorithm for choosing a path maximizing diffusion. The latter problem is resolved by kinetic Monte Carlo (KMC), which generates multiple paths through the network of Tyr and Trp residues and yields the time of first passage between the injection and collection sites. However, it does not provide a direct formalism for calculating the diffusion coefficient. The ability of the carriers to transverse the 3D protein over many alternative paths is an essential aspect of the problem that has to be captured by a successful formalism. In the absence of such a formulation, we adopted a somewhat heuristic extension of the result for a Brownian walker (to which Derrida's model reduces for symmetric forward and backward rates), calculating the diffusion constant in the form

$$D = \left\langle \frac{(\Delta x)^2}{2\tau} \right\rangle$$

where both the step size Δx and the step time τ are stochastic variables changing along the paths produced by KMC. Specifically, τ is calculated as the waiting time on a given site.

https://doi.org/10.1021/acsphyschemau.3c00017
ACS Phys. Chem Au 2023, 3, 444−455

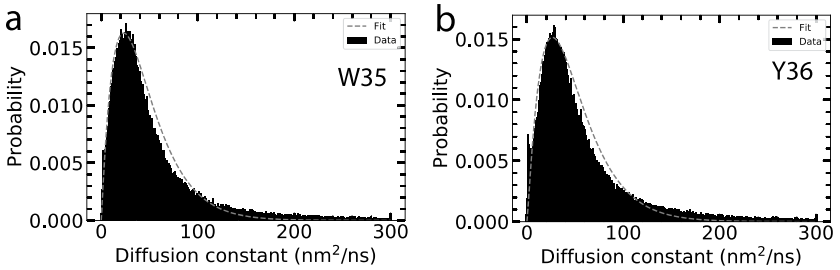

Figure 6. Distribution of diffusion constant values for paths that connect W35 and Y89 (a) and Y36 and Y89 (b) calculated via a kinetic Monte Carlo algorithm. Fitting with Gamma distribution functions (dashed lines) yields most probable values of D = 22.1 nm^2/ns for the W35 paths and 22.8 nm^2/ns for the Y36 paths.

In the limit of a single path, this result reduces to Deridda's calculation, where the average is now for the sites along the path. In the KMC formulation, the average was taken along a given path, with the most probable value of diffusion constant given by the peak of the distribution calculated for all paths.

The calculation is set up using the hopping rates and center-of-mass distances (Table S2) for all aromatic pairs within a Dutton radius in two repeats of the CTPR unit. We use two repeats so as to include the hops between neighboring repeats (cf., Figure 2b). As shown in Figure S1, the properties of longer proteins are captured via translational symmetry.

Using the data listed in Table S2, a graph was constructed with edges that represent the hopping rates, with two edges between each pair of residues, one representing the forward hopping rate and the second representing the backward hopping rate. Electron hopping MC simulations were run until the electron reached the exit residue, with the value of D_i calculated at the ith hop from the residence time, τ_i, and the center of mass hopping distance Δx_i. On completion of the passage, an average of these values is stored (eqs S17−S21).

In the experiments, N- and C-terminal cysteines were incorporated into the proteins in order to form defined chemical contacts to the electrodes. Examination of the structure (Figure 2b) shows that C- terminal injection or extraction is only likely at Y89.

Injection at the N-terminal can occur at W35 (the closest residue in sequence to the N terminus) or Y36 which is at almost the same through-space edge-to-edge distance (0.9 nm) from the cysteine (W35 is 1 nm through-space edge-to-edge distance from the cysteine). We have therefore calculated the distribution of D values for paths that start or end on either of these residues (the inclusion of backward and forward hops captures diffusion in either direction). 100,000 simulations were run for each set of paths, and the distributions of D are shown in Figure 6a (W35 path) and 6b (Y36 path). The corresponding most probable D values are 22.1 and 22.8 nm^2/ns.

As a check on this heuristic approach, we used the Derrida formalism[58] to calculate values for two limiting cases. In one case, we chose a single path that maximized forward rates (which is not the same as maximizing the diffusion constant) and calculated the corresponding diffusion constant (this path illustrated in Figure 2b). The calculation was carried out following eqs S13 and S14 using the rates shown in Table S3 (the final hop that closes the loop as required for the Derrida theory is Y89 to W35, equivalent to Y89 to W103 owing to translational symmetry—Figure S1). For this path, we obtain D = 3.06 nm^2/ns, an order of magnitude less than the multiple-path value obtained from the KMC calculations. An alternative approach, using the Derrida theory, is to find all the paths that connect the entry and exit, to calculate the corresponding D values for each, and then summing them on the assumption that each path adds a current proportional to its corresponding D. The obvious fault with this approach is that paths are allowed to overlap—i.e., this approach allows a given site to be multiply oxidized (which is energetically highly unlikely). This will yield an overestimate of D. We find 433 such paths connecting Y36 to Y89 for which the total D = 578 nm^2/ns, an order of magnitude larger than the value obtained from the MC calculations. These two limiting cases bound the results of the MC simulations, indicating that our heuristic calculation of D from KMC is likely of the correct order of magnitude.

Charge Injection

We assume charge injection into a single site for which the injection and recombination rates depend only on the potential drop at the contacts, η (Figure 5a), and the electronic coupling between the electrodes and the entry and exit sites, assumed, for simplicity, to be the same, Δ eV, at each contact. Using empirical data to calculate η (Figure S2) and expressions for the injection rates (eq S15) solved for stationary conditions (eqs S14−S16) results in the following expression for the contact conductance

$$G_0 = \left.\frac{\mathrm{d}I}{\mathrm{d}\eta}\right|_{\eta=0} = \frac{2e^2\Delta}{\hbar\sqrt{\pi\lambda^{\mathrm{r}}k_{\mathrm{B}}T}}\exp\left[-\frac{\lambda^{\mathrm{r}}}{4k_{\mathrm{B}}T}\right] \tag{7}$$

Evaluating this expression for λ^{r} = 0.16 eV and a measured contact conductance of 4.55 nS (1/220 MΩ) yields $\Delta = 5 \times 10^{-6}$ eV. This coupling has also been evaluated for electron transfer from an electrode to cytochrome c supported on a hydrocarbon monolayer using electrochemical data, yielding, in that case,[59] $\Delta = 1.4 \times 10^{-6}$ eV, similar enough to the value for Δ obtained from eq 7 to imply that the fitted value is not entirely arbitrary.

Stationary Current

The stationary current through the protein can be written in terms of the fraction of oxidized states at each contact n_i and the diffusion flux j_{d} of charge carriers through the protein with n_i satisfying the following current balance conditions

$$\begin{aligned} -n_1k_{\mathrm{R}}^1c_{\mathrm{s}} + (1-n_1)k_{\mathrm{O}}^1c_{\mathrm{s}} - J_{\mathrm{d}} &= 0 \\ -n_2k_{\mathrm{R}}^2c_{\mathrm{s}} + (1-n_2)k_{\mathrm{O}}^2c_{\mathrm{s}} + J_{\mathrm{d}} &= 0 \end{aligned} \tag{8}$$

where $J_{\mathrm{d}} = -D\cdot\partial_x\rho(x)$ is the diffusional flux due to the gradient of the bulk number density $\rho(x)$ and D is the diffusion constant calculated above. Expressing the rates $k_{\mathrm{R}}^{1,2}$ and $k_{\mathrm{O}}^{1,2}$ (eq S15) in the dimensionless form leads to

https://doi.org/10.1021/acsphyschemau.3c00017
ACS Phys. Chem Au 2023, 3, 444−455

$$J_d/J_0 = -a\frac{\delta}{L}[n_2 - n_1] \tag{9}$$

where $J_0 = c_s\Delta/\hbar = \Delta/(\hbar S)$ and S is the contact area. The saturation current is given by $I_0 = eJ_0S = e\Delta/\hbar \approx 1.2$ nA (using $\Delta = 5 \times 10^{-6}$ eV). The dimensionless parameter a is given by

$$a = \frac{D\hbar}{\delta^2\Delta} \tag{10}$$

Here, δ is the size of the entry/exit residue (adopted as 0.96 nm, representative of the two residues). With the values of D calculated above (22.1−22.8 nm^2/ns), we obtain $a = 3.12-3.22$. Eqs 8 and 9 can be solved for n_1 and n_2 to produce the diffusive current of holes and the corresponding conductivity

$$n_1 = \frac{k_O^1 + \frac{a}{l}\frac{k_O^1 + k_O^2}{k^2}}{k^1 + \frac{a}{l}\left(1 + \frac{k^1}{k^2}\right)}$$

$$n_2 = \frac{k_O^2 + \frac{a}{l}\frac{k_O^1 + k_O^2}{k^1}}{k^2 + \frac{a}{l}\left(1 + \frac{k^2}{k^1}\right)} \tag{11}$$

where $k^1 = k_O(\eta) + k_R(\eta)$ and $k^2 = k_O(-\eta) + k_R(-\eta)$, as calculated from eqs S14, and $l = L/\delta$.

Equation 11 provides the solution for the stationary current through the protein

$$\frac{I(V_b, l)}{I_0} = -\frac{a}{l}[n_2(\eta, l) - n_1(\eta, l)] \tag{12}$$

where the dependence of η on V_b and l is given in the caption of Figure S2. Figure 5b plots $\frac{I(V_b, l)}{I_0}$ vs V_b for two protein lengths (10 and 15 nm). With $I_0 \approx 1.2$ nA (as calculated from the contact resistance above), the calculated $I-V$ curves are of the same magnitude as the examples given in Figure 1c and feature a linear regime in the ±200 mV range as observed experimentally.

The resistance as a function of l is given by

$$R = \left[\frac{\partial I(V_b, l)}{\partial \eta}\frac{\partial \eta}{\partial V_b}\bigg|_{V_b=0}\right]^{-1} \tag{13}$$

The conductivity R^{-1} was fitted to the experimental data, and the fit and data (squares) are shown as a function of resistance in Figure 5c to allow comparison with Figure 1d. The best fit parameter $a = 3.8$, close to the values (3.12−3.22) calculated above, showing that the present approach correctly predicts the current decay with distance. In a previous experimental work,[3] the non-linear dependence of the molecular resistance on length was hypothesized to be intrinsic to the diffusion process. The analysis presented here predicts an inherently linear dependence, as it must be, given that the current is proportional to the carrier velocity, i.e., the ratio of diffusion time to molecular length. The observed non-linearity is mostly accounted for by the dependence of the potential distribution on the length of the molecule.

The absolute magnitude of the current is determined by I_0 which was calculated to be 1.2 nA via the estimate of the electronic coupling constant, Δ, a parameter that the decay rate (eq 10) also depends on. This estimate is based on the assumption of equal resistance of two contacts which can be merged into one residue to calculate the contact resistance. The fit to the resistance data (which are based on the peak of the distributions obtained from many current−voltage curves) is based instead on evaluating the diffusive current in eqs 9 and 12 and required $I_0 = 5.5$ nA, ∼4× the value obtained from Δ, but nonetheless surprisingly close, given the limitations of the contact model. Thus, while the absolute values of current depend on the fitted parameter Δ, its value is not entirely arbitrary, being consistent with a value obtained from electrochemical measurements.[59]

The rather precise agreement between the calculated decay rate $a = 3.12-3.22$ and the value obtained from experimental data ($a = 3.8$) is probably fortuitous, given both the lack of an exact theory for the diffusion process and other approximations used here: the force fields employed in MD are non-polarizable and thus neglect screening of charges by induced molecular dipoles. An indication that this can cause minor inconsistencies is the fact that the mean ratio $\langle\lambda^{St}/\lambda\rangle \approx 0.4$ is somewhat higher than ≈0.3 from comparing eq 3 with the position of the conductance peak in Figure 1e. Dynamical heterogeneity, in particular, at sites closer to the protein−water interface can lead to faster dynamics and, correspondingly, to lower $g(R)$, as shown in eq 4. Despite these limitations, the present theory demonstrates how long-range hopping is enabled through a reduced reorganization energy owing to non-ergodicity. The theory accurately predicts the decay of current with the length of the proteins and fits the absolute magnitude of current with a reasonable value for the coupling constant, Δ.

Limitations of the Present Model

Delocalized valence-band orbitals have been offered as an alternative explanation for long-range conductance in dry multiheme proteins, where it is proposed that the transmission is via direct tunneling across the whole protein with a very small effective decay constant.[60,61] In the case of the multiheme wires, OmcS[62] and OmcZ,[63] a small shift in heme−heme separation causes a thousand-fold change in conductance, suggestive of significant delocalization effects or changes in contact resistance. The timescales of localized medium vibrations and charge tunneling, $\hbar/V$, overlap in the protein studied here (see below) likely trapping the charge at the hopping sites and limiting quantum coherence and delocalization. Our simulations extend only to the sub-microsecond time scale, not reaching into the timescale of the protein motions that occur over many microseconds. These slower relaxations are the source of the non-ergodicity because, as the simulations show, charge transfer occurs on the ns or shorter timescales. In order to investigate the involvement of faster relaxations, we calculated the Stokes-shift loss spectrum[64,65] from the Stokes-shift dynamics generated by the simulations (Figure S6). The figure shows that most of the relaxation of electrostatic interactions occurs on a time-scale shorter than the reaction time, which is consistent with the Stokes-shift integral relaxation time of 20 ps. However, the faster reaction rates cut through the relaxation peak of the slower relaxation process. In order to treat this process correctly, a full propagation of quantum-mechanical population and medium dynamics is needed (as done, for example, in a recent treatment of DNA photolyase[45]). Such simulations are presently limited by time scales much shorter than those required to sample the statistics of the energy-gap reaction coordinate. We expect some reduction of the effective reorganization energy through a dynamic non-ergodicity parameter that corrects for the reduced range of frequencies

https://doi.org/10.1021/acsphyschemau.3c00017
ACS Phys. Chem Au 2023, 3, 444−455

$$f_{na} = \int_k^\infty \frac{d\omega}{\pi\omega}\chi''(\omega) / \int_0^\infty \frac{d\omega}{\pi\omega}\chi''(\omega)$$

From the spectrum shown in Figure S6, we obtain $f_{na} \simeq 0.85$ for $k = 1$ ns^{-1} and $f_{na} \simeq 0.75$ for $k = 10$ ns^{-1}. However, the dynamic non-ergodicity parameter should multiply both λ^{St} and λ, and thus, λ^r (eq 2) should be replaced with $f_{na}\cdot\lambda^r$. Given these estimates, our results for the reaction reorganization energy are most likely upper bound values. Since we have not calculated the Stokes shift dynamics for all hops, this formalism cannot be consistently applied to all calculated conductivity steps.

CONCLUSIONS

The key result of this work is that proteins that do not contain redox cofactors, but that have an adequate density of aromatic residues, can support long-range and rapid hopping of electrons, with implications for the role of aromatic amino acids in facilitating charge transport. The same reduction of reorganization energy that accounts for this long-range transport also largely accounts for the alignment of the non-equilibrium charge shift states with the Fermi energy of some noble metals, important for the use of proteins as bioelectronic components. The reorganization energy (corrected for electronic screening) appropriate to non-equilibrium oxidation states of tyrosine and tryptophan, ∼0.16 eV, is significantly smaller than the Marcus reorganization energy derived from the Stokes shift (∼0.8 eV). This reduced reorganization energy corresponds to a barrier (for $\Delta G = 0$) of 40 meV, which is close to available kinetic thermal energy $(3/2)kT$. This reduction of reorganization energy has previously been demonstrated for charge transfer between cofactors[22,24,25,27,30,31] and is now extended to the aromatic amino acids. Even in the case of proteins rich in cofactors, the origin of the required reduction in reorganization energy remains obscure,[15] so it is interesting to note that a reorganization energy below 0.2 eV and a fast diffusion constant (>20 nm^2/ns), the conditions required for fast transport in OmcS proteins, are obtained in the present case for transport in a protein that lacks any redox cofactors. In addition, this reduction of the reorganization energy provides a plausible explanation for the fact that the current-carrying states appear to be some 700 mV closer to the vacuum (i.e., at 300 mV vs NHE) than would be expected from the equilibrium oxidation potentials of tyrosine and tryptophan (1 V vs NHE). Although we have fitted the current−voltage curves using a parameter, Δ, derived from the measured contact resistance, the value obtained for Δ is of the same order of magnitude for this coupling parameter as derived from electrochemical data for another protein, indicating that our model yields the correct order of magnitude for the absolute currents.

METHODS

MD Protocols

All MD simulations were performed using NAMD2[66] periodic boundary conditions, the CHARMM36 force field[67] for the protein, and the TIP3P model[68] for water. Van der Waals and short-range electrostatic forces were evaluated using a 1.2 nm cutoff, whereas long-range electrostatic forces were evaluated using the particle mesh Ewald method computed over a 0.12 nm-spaced grid.[43] The initial equilibration of the CTPR8 system was performed using a 2 fs time step. Simulations of the CTPR8 systems containing an oxidized residue were performed using a 4 fs integration time step and the hydrogen mass repartition scheme.[44] Results were consistent with calculations using a 2 fs step and the standard hydrogen mass. The equilibration simulations were performed in the constant number of particles, pressure (1 bar), and temperature (310 K) ensemble maintained using a Langevin dynamics thermostat and the Nose−Hoover Langevin pressure control.[69,70] Visualization and analysis were performed using VMD.[43]

MD Simulations of CTPR8 Systems

The atomic coordinates of a CTPR8 protein were taken from the published crystal structure.[71] To reproduce the protein construct used in experiment,[3] the N and C termini of the protein were extended by 31 and 18 amino acids, respectively, both terminating with a cysteine residue. The partially folded structure of the N-terminal addition was generated using the Iterative Threading ASSEmbly Refinement (I-TASSER) server (Zhang lab, University of Michigan) and its default parameters,[72] and the C-terminal addition was assumed to be disordered. The resulting atomic model of the experimental CTPR8 protein is provided in the Supporting Information, CTPR8-Cys.pdb. Missing hydrogen atoms were added to the protein using the psfgen plugin of VMD. The protein was immersed in a $8.0 \times 8.6 \times 7.1$ nm^3 pre-equilibrated volume of water using the Solvate Plugin of VMD.[73] Potassium and chloride ions were added using the Autoionize plugin to produce 150 mM KCl solution. The system was minimized using the conjugate gradient method for 100 steps, which was followed by a 500 ns equilibration run. During the first 25 ns of the equilibration, the C_α atoms of the protein were restrained to their initial coordinates using harmonic potentials with a force constant of 100 kcal/(mol nm^2). The microscopic configuration of the CTPR8 system obtained at the end of the 500 ns equilibration was used to construct thirteen CTPR8 systems each containing a different tryptophan or tyrosine residue in its oxidized state. These tyrosine and tryptophan residues were assumed to be oxidized to their cationic free radical state, carrying an overall charge of one proton. The partial charges of an oxidized tyrosine or an oxidized tryptophan residue were taken from previous semi-empirical[35] and quantum mechanics/molecular mechanics (QM/MM)[41] calculations, respectively. The patches used to oxidize the residues are provided in the Supporting Information (oxidize_Y.txt and oxidize_W.txt), and the values of the partial charges are listed in Tables S4 and S5. Each system containing an oxidized residue was then equilibrated for 750 ns. Atomic coordinates were saved every 10 ps.

Calculation of the Electrostatic Potential at the Active Residue

To calculate the energy-gap trajectory, we evaluated the electrostatic potentials at the location of the atoms of the redox-active residue every 10 ps using the method[43] implemented in the PMEpot Plugin of VMD.

The resulting electrostatic potentials Φ_j at the location of atoms j (atoms whose charge changes during the charge transition) were extracted from the MD simulation of the oxidized and reduced residues. The electrostatic (Coulomb) component of the donor−acceptor energy gap was calculated as

$$X^C = -\sum_j \Delta q_j^{\,D}\Phi_j + \sum_j \Delta q_j^{\,A}\Phi_j \tag{14}$$

where $\Delta q_j^a = q_j^{a,red} - q_j^{a,ox}$ are differences of atomic charges in the reduced and oxidized states of the donor, a = D, and acceptor, a = A, moieties.

The Stokes-shift reorganization energy is given by the difference of average values of the energy gap in the initial and final charge-transfer states

$$2\lambda^{St} = \langle X\rangle_1 - \langle X\rangle_2 \tag{15}$$

The average $\langle X\rangle_1$ was calculated from MD simulation of the reduced donor and reduced acceptor, whereas $\langle X\rangle_2$ was calculated from MD simulation of the oxidized donor and oxidized acceptor (see Figure 2c for the reaction diagram). The variance reorganization energy λ was determined as the mean of the energy-gap variances $\lambda_i = \sigma_{X,i}^{\,2}/2k_BT$: $\lambda = (\lambda_1 + \lambda_2)/2$. The hopping rates (Table S2) were calculated according to eqs 4 and 5.

Evaluation of the Dynamic Crossover Parameter *g*

The parameter g is given by[49]

https://doi.org/10.1021/acsphyschemau.3c00017
ACS Phys. Chem Au 2023, 3, 444−455

$$g = \frac{2\pi V_{DA}^2 \tau_X}{\sigma_X \hbar} \frac{\exp\left(\frac{3}{2}\gamma^2 \langle (\delta R)^2 \rangle\right)}{\sqrt{2\Delta G^{\ddagger}/k_B T + 4(\tau_X/\tau_R)\gamma^2 \langle (\delta R)^2 \rangle}} \quad (16)$$

where $\Delta G^{\ddagger}$ is given by eq 1 in which λ is replaced with λ^r and the reaction free energy is from eq 3, $\sigma_X^2 = 2k_B T\lambda$, and τ_X and τ_R are the relaxation times of the Stokes-shift dynamics and of the donor−acceptor distance, respectively. The integrated relaxation times $\tau_{X,R}$ were calculated using the time correlation functions from MD (Figures S3 and S4 and eqs S6 and S7).

■ ASSOCIATED CONTENT

Supporting Information

The Supporting Information is available free of charge at https://pubs.acs.org/doi/10.1021/acsphyschemau.3c00017.

Fluctuations in equivalent residues, bias distribution, Stokes shift dynamics, test of the Hopfield equation, polarizability, rate calculations, Derrida model, charge injection model, kinetic Monte Carlo calculations, Stokes shift loss spectrum, and tables of rates, couplings, and partial charges (PDF)

Atomic model of the experimental CTPR8 protein (PDB)

Patch for oxidizing tyrosine (TXT)

Patch for oxidizing tryptophan (TXT)

■ AUTHOR INFORMATION

Corresponding Authors

Aleksei Aksimentiev − *Department of Physics and Beckman Institute for Advanced Science and Technology, University of Illinois at Urbana-Champaign, Urbana, Illinois 61801, United States;* orcid.org/0000-0002-6042-8442; Email: aksiment@illinois.edu

Stuart Lindsay − *Department of Physics, Arizona State University, Tempe, Arizona 85281, United States; School of Molecular Sciences and Biodesign Institute, Arizona State University, Tempe, Arizona 85281, United States;* orcid.org/0000-0002-9364-6542; Email: Stuart.Lindsay@asu.edu

Dmitry Matyushov − *Department of Physics, Arizona State University, Tempe, Arizona 85281, United States; School of Molecular Sciences, Arizona State University, Tempe, Arizona 85281, United States;* Email: dmatyus@asu.edu

Author

Siddharth Krishnan − *Department of Physics and Beckman Institute for Advanced Science and Technology, University of Illinois at Urbana-Champaign, Urbana, Illinois 61801, United States*

Complete contact information is available at: https://pubs.acs.org/10.1021/acsphyschemau.3c00017

Author Contributions

The manuscript was written through contributions of all authors. All authors have given approval to the final version of the manuscript.

Funding

This work was supported by grant 1R01HG011079 from the National Human Genome Research Institute, grant CHE-2154465 from the National Science Foundation, grant W911NF2010320 from the US Army and the Edward and Nadine Carson Endowment. A.A. acknowledges support via grants from the National Science Foundation (PHY-1430124 and DMR-1827346). The supercomputer time was provided through the Extreme Science and Engineering Discovery Environment (XSEDE) allocation MCA05S028.

Notes

The authors declare the following competing financial interest(s): SL is a cofounder of a company with interests in this the subject matter of the present paper.

■ ACKNOWLEDGMENTS

We thank E.R. for generating the protein structures.

■ REFERENCES

(1) Nicholls, D. G.; Ferguson, S. J. *Bioenergetics*; Academic Press: Amsterdam, 2013; Vol. *4*.

(2) Zhang, B.; Song, W.; Pang, P.; Lai, H.; Chen, Q.; Zhang, P.; Lindsay, S. The Role of Contacts in Long-Range Protein Conductance. *Proc. Natl. Acad. Sci. U.S.A.* **2019**, *116*, 5886−5891.

(3) Zhang, B.; Ryan, E.; Wang, X.; Song, W.; Lindsay, S. Electronic Transport in Molecular Wires of Precisely Controlled Length Built from Modular Proteins. *ACS Nano* **2022**, *16*, 1671−1680.

(4) Stubbe, J.; Nocera, D. G.; Yee, C. S.; Chang, M. C. Radical initiation in the class I ribonucleotide reductase: long-range proton-coupled electron transfer? *Chem. Rev.* **2003**, *34*, 2167−2201.

(5) Bollinger, M. J. Electron Relay in Proteins. *Science* **2008**, *320*, 1730−1731.

(6) Shih, C.; Museth, A. K.; Abrahamsson, M.; Blanco-Rodriguez, A. M.; Di Bilio, A. J.; Sudhamsu, J.; Crane, B. R.; Ronayne, K. L.; Towrie, M.; Vlček, A.; Richards, J. H.; Winkler, J. R.; Gray, H. B. Tryptophan-accelerated electron flow through proteins. *Science* **2008**, *320*, 1760−1762.

(7) Gray, H. B.; Winkler, J. R. Hole hopping through tyrosine/tryptophan chains protects proteins from oxidative damage. *Proc. Natl. Acad. Sci. U.S.A.* **2015**, *112*, 10920−10925.

(8) Beratan, D. N.; Betts, J. N.; Onuchic, J. N. Protein electron transfer rates set by the bridging secondary and tertiary structure. *Science* **1991**, *252*, 1285−1288.

(9) Page, C. C.; Moser, C. C.; Chen, X.; Dutton, P. L. Natural engineering principles of electron tunnelling in biological oxidation-reduction. *Nature* **1999**, *402*, 47−52.

(10) Marcus, R. A.; Sutin, N. Electron transfers in chemistry and biology. *Biochem. Biophys. Acta* **1985**, *811*, 265−322.

(11) Winkler, J. R.; Gray, H. B. Electron flow through metalloproteins. *Chem. Rev.* **2014**, *114*, 3369−3380.

(12) Close, D. M. Calculated vertical ionization energies of the common alpha-amino acids in the gas phase and in solution. *J. Phys. Chem. A* **2011**, *115*, 2900−2912.

(13) Ing, N. L.; El-Naggar, M. Y.; Hochbaum, A. I. Going the Distance: Long-Range Conductivity in Protein and Peptide Bioelectronic Materials. *J. Phys. Chem. B* **2018**, *122*, 10403−10423.

(14) Shipps, C.; Kelly, H. R.; Dahl, P. J.; Yi, S. M.; Vu, D.; Boyer, D.; Glynn, C.; Sawaya, M. R.; Eisenberg, D.; Batista, V. S.; Malvankar, N. S. Intrinsic electronic conductivity of individual atomically resolved amyloid crystals reveals micrometer-long hole hopping via tyrosines. *Proc. Natl. Acad. Sci. U.S.A.* **2021**, *118*, No. e2014139118.

(15) Eshel, Y.; Peskin, U.; Amdursky, N. Coherence-assisted electron diffusion across the multi-heme protein-based bacterial nanowire. *Nanotechnology* **2020**, *31*, 314002.

(16) Zhang, B.; Song, W.; Brown, J.; Nemanich, R.; Lindsay, S. Electronic Conductance Resonance in Non-Redox-Active Proteins. *J. Am. Chem. Soc.* **2020**, *142*, 6432−6438.

(17) Harriman, A. Further comments on the redox potentials of tryptophan and tyrosine. *J. Phys. Chem.* **1987**, *91*, 6102−6104.

(18) Odella, E.; Mora, S. J.; Wadsworth, B. L.; Huynh, M. T.; Goings, J. J.; Liddell, P. A.; Groy, T. L.; Gervaldo, M.; Sereno, L. E.; Gust, D.; Moore, T. A.; Moore, G. F.; Hammes-Schiffer, S.; Moore, A. L. Controlling Proton-Coupled Electron Transfer in Bioinspired Artificial Photosynthetic Relays. *J. Am. Chem. Soc.* **2018**, *140*, 15450−15460.

(19) Warshel, A. Dynamics of reactions in polar solvents. Semiclassical trajectory studies of electron-transfer and proton-transfer reactions. *J. Phys. Chem.* **1982**, *86*, 2218−2224.
(20) Kubo, R. The fluctuation-dissipation theorem. *Rep. Prog. Phys.* **1966**, *29*, 255−284.
(21) Landau, L. M.; Lifshits, E. M. *Statistical Physics*; Pergammon Press: New York, 1980.
(22) Matyushov, D. V. Protein electron transfer: Dynamics and statistics. *J. Chem. Phys.* **2013**, *139*, 025102.
(23) Frauenfelder, H.; Chen, G.; Berendzen, J.; Fenimore, P. W.; Jansson, H.; McMahon, B. H.; Stroe, I. R.; Swenson, J.; Young, R. D. A unified model of protein dynamics. *Proc. Natl. Acad. Sci. U.S.A.* **2009**, *106*, 5129−5134.
(24) Matyushov, D. V. Protein electron transfer: is biology (thermo)dynamic? *J. Phys.: Condens. Matter* **2015**, *27*, 473001.
(25) Martin, D. R.; Matyushov, D. V. Communication: Microsecond dynamics of the protein and water affect electron transfer in a bacterial bc(1) complex. *J. Chem. Phys.* **2015**, *142*, 161101.
(26) Kontkanen, O. V.; Biriukov, D. A.-O.; Futera, Z. A.-O. Reorganization free energy of copper proteins in solution, in vacuum, and on metal surfaces. *J. Chem. Phys.* **2022**, *156*, 175101.
(27) Barragan, A. M.; Soudackov, A. V.; Luthey-Schulten, Z.; Hammes-Schiffer, S.; Schulten, K.; Solov'yov, I. A. Theoretical Description of the Primary Proton-Coupled Electron Transfer Reaction in the Cytochrome bc1 Complex. *J. Am. Chem. Soc.* **2021**, *143*, 715−723.
(28) Dahl, P. J.; Yi, S. M.; Gu, Y.; Acharya, A. A.-O.; Shipps, C. A.-O.; Neu, J. A.-O.; O'Brien, J. P.; Morzan, U. N.; Chaudhuri, S. A.-O.; Guberman-Pfeffer, M. J.; Vu, D. A.-O. X.; Yalcin, S. E.; Batista, V. S.; Malvankar, N. S. A 300-fold conductivity increase in microbial cytochrome nanowires due to temperature-induced restructuring of hydrogen bonding networks. *Sci. Adv.* **2022**, *8*, No. eabm 7913.
(29) Guberman-Pfeffer, M. J. Assessing Thermal Response of Redox Conduction for Anti-Arrhenius Kinetics in a Microbial Cytochrome Nanowire. *J. Phys. Chem. B* **2022**, *126*, 10083−10097.
(30) Dahl, P. J.; Yi, S. M.; Gu, Y.; Acharya, A.; Shipps, C.; Neu, J.; O'Brien, J. P.; Morzan, U. N.; Chaudhuri, S.; Guberman-Pfeffer, M. J.; Vu, D.; Yalcin, S. E.; Batista, V. S.; Malvankar, N. S. A 300-fold conductivity increase in microbial cytochrome nanowires due to temperature-induced restructuring of hydrogen bonding networks. *Sci. Adv.* **2022**, *8*, No. eabm7193.
(31) Husen, P.; Solov'yov, I. A. Modeling the Energy Landscape of Side Reactions in the Cytochrome bc1 Complex. *Front. Chem.* **2021**, *9*, 9.
(32) Zhang, B.; Lindsay, S. Electronic Decay Length in a Protein Molecule. *Nano Lett.* **2019**, *19*, 4017−4022.
(33) Fereiro, J. A.; Yu, X.; Pecht, I.; Sheves, M.; Cuevas, J. C.; Cahen, D. Tunneling explains efficient electron transport via protein junctions. *Proc. Natl. Acad. Sci. U.S.A.* **2018**, *115*, E4577−E4583.
(34) Kayser, B.; Fereiro, J. A.; Bhattacharyya, R.; Cohen, S. R.; Vilan, A.; Pecht, I.; Sheves, M.; Cahen, D. Solid-State Electron Transport via the Protein Azurin is Temperature-Independent Down to 4 K. *J. Phys. Chem. Lett.* **2020**, *11*, 144−151.
(35) Romero-Muñiz, C.; Ortega, M.; Vilhena, J. G.; Díez-Pérez, I.; Pérez, R.; Cuevas, J. C.; Zotti, L. A. Can Electron Transport through a Blue-Copper Azurin Be Coherent? An Ab Initio Study. *J. Phys. Chem. C* **2021**, *125*, 1693−1702.
(36) Irebo, T.; Johansson, O.; Hammarström, L. The Rate Ladder of Proton-Coupled Tyrosine Oxidation in Water: A Systematic Dependence on Hydrogen Bonds and Protonation State. *J. Am. Chem. Soc.* **2008**, *130*, 9194−9195.
(37) Nilsen-Moe, A.; Rosichini, A.; Glover, S. D.; Hammarström, L. Concerted and Stepwise Proton-Coupled Electron Transfer for Tryptophan-Derivative Oxidation with Water as the Primary Proton Acceptor: Clarifying a Controversy. *J. Am. Chem. Soc.* **2022**, *144*, 7308−7319.
(38) Müller, P. A.-O.; Ignatz, E.; Kiontke, S. A.-O. X.; Brettel, K. A.-O.; Essen, L. O. Sub-nanosecond tryptophan radical deprotonation mediated by a protein-bound water cluster in class II DNA photolyases. *Chem. Sci.* **2018**, *9*, 1200−1212.
(39) Shafaat, H. S.; Leigh, B. S.; Tauber, M. J.; Kim, J. E. Spectroscopic Comparison of Photogenerated Tryptophan Radicals in Azurin: Effects of Local Environment and Structure. *J. Am. Chem. Soc.* **2010**, *132*, 9030−9039.
(40) Aubert, C.; Vos, M. H.; Mathis, P.; Eker, A. P. M.; Brettel, K. Intraprotein radical transfer during photoactivation of DNA photolyase. *Nature* **2000**, *405*, 586−590.
(41) Popovic, D. M.; Zmiric, A.; Zaric, S. D.; Knapp, E. W. Energetics of radical transfer in DNA photolyase. *J. Am. Chem. Soc.* **2002**, *124*, 3775−3782.
(42) Bernini, C.; Pogni, R.; Ruiz-Duenas, F. J.; Martinez, A. T.; Basosi, R.; Sinicropi, A. EPR parameters of amino acid radicals in P. eryngii versatile peroxidase and its W164Y variant computed at the QM/MM level. *Phys. Chem. Chem. Phys.* **2011**, *13*, 5078−5098.
(43) Aksimentiev, A.; Schulten, K. Imaging alpha-hemolysin with molecular dynamics: ionic conductance, osmotic permeability, and the electrostatic potential map. *Biophys. J.* **2005**, *88*, 3745−3761.
(44) Balusek, C.; Hwang, H.; Lau, C. H.; Lundquist, K.; Hazel, A.; Pavlova, A.; Lynch, D. L.; Reggio, P. H.; Wang, Y.; Gumbart, J. C. Accelerating Membrane Simulations with Hydrogen Mass Repartitioning. *J. Chem. Theory Comput.* **2019**, *15*, 4673−4686.
(45) Lüdemann, G.; Woiczikowski, P. B.; Kubař, T.; Elstner, M.; Steinbrecher, T. B. Charge Transfer in E. coli DNA Photolyase: Understanding Polarization and Stabilization Effects via QM/MM Simulations. *J. Phys. Chem. B* **2013**, *117*, 10769−10778.
(46) Matyushov, D. V. Reorganization energy of electron transfer. *Phys. Chem. Chem. Phys.* **2023**, *25*, 7589−7610.
(47) Cailliez, F.; Müller, P.; Firmino, T.; Pernot, P.; de la Lande, A. Energetics of Photoinduced Charge Migration within the Tryptophan Tetrad of an Animal (6−4) Photolyase. *J. Am. Chem. Soc.* **2016**, *138*, 1904−1915.
(48) Blumberger, J. Free energies for biological electron transfer from QM/MM calculation: method, application and critical assessment. *Phys. Chem. Chem. Phys.* **2008**, *10*, 5651−5667.
(49) Matyushov, D. V. Conformational dynamics modulating electron transfer, 2022, arXiv:2207.08753 (Biological Physics). https://arxiv.org/abs/2207.08753 (accessed July 18, 2022).
(50) Zusman, L. D. Outer-sphere electron transfer in polar solvents. *Chem. Phys.* **1980**, *49*, 295−304.
(51) Rips, I.; Jortner, J. Dynamic solvent effects on outer-sphere electron transfer. *J. Chem. Phys.* **1987**, *87*, 2090−2104.
(52) Heitele, H. Dynamic Solvent Effects on Electron-Transfer Reactions. *Angew. Chem., Int. Ed. Engl.* **1993**, *32*, 359−377.
(53) Beratan, D. N.; Liu, C.; Migliore, A.; Polizzi, N. F.; Skourtis, S. S.; Zhang, P.; Zhang, Y. Charge transfer in dynamical biosystems, or the treachery of (static) images. *Acc. Chem. Res.* **2015**, *48*, 474−481.
(54) Hopfield, J. J. Electron Transfer Between Biological Molecules by Thermally Activated Tunneling. *Proc. Natl. Acad. Sci. U.S.A.* **1974**, *71*, 3640−3644.
(55) Teo, R. D.; Rousseau, B. J. G.; Smithwick, E. R.; Di Felice, R.; Beratan, D. N.; Migliore, A. Charge Transfer between [4Fe4S] Proteins and DNA Is Unidirectional: Implications for Biomolecular Signaling. *Chem* **2019**, *5*, 1682−1684.
(56) Teo, R. D.; Wang, R.; Smithwick, E. R.; Migliore, A.; Therien, M. J.; Beratan, D. N. Mapping hole hopping escape routes in proteins. *Proc. Natl. Acad. Sci. U.S.A.* **2019**, *116*, 15811−15816.
(57) Martin, D. R.; Dinpajooh, M.; Matyushov, D. V. Polarizability of the Active Site in Enzymatic Catalysis: Cytochrome c. *J. Phys. Chem. B* **2019**, *123*, 10691−10699.
(58) Derrida, B. Velocity and diffusion constant of a one-dimenional hopping model. *J. Stat. Phys.* **1983**, *31*, 433−450.
(59) Seyedi, S. S.; Waskasi, M. M.; Matyushov, D. V. Theory and Electrochemistry of Cytochrome c. *J. Phys. Chem. B* **2017**, *121*, 4958−4967.
(60) Futera, Z.; Ide, I.; Kayser, B.; Garg, K.; Jiang, X.; van Wonderen, J. H.; Butt, J. N.; Ishii, H.; Pecht, I.; Sheves, M.; Cahen, D.; Blumberger, J. Coherent Electron Transport across a 3 nm Bioelectronic Junction

Made of Multi-Heme Proteins. *J. Phys. Chem. Lett.* **2020**, *11*, 9766−9774.
(61) Futera, Z.; Wu, X.; Blumberger, J. Tunneling-to-Hopping Transition in Multiheme Cytochrome Bioelectronic Junctions. *J. Phys. Chem. Lett.* **2023**, *14*, 445−452.
(62) Wang, F.; Gu, Y.; O'Brien, J. P.; Yi, S. M.; Yalcin, S. E.; Srikanth, V.; Shen, C.; Vu, D.; Ing, N. L.; Hochbaum, A. I.; Egelman, E. H.; Malvankar, N. S. Structure of Microbial Nanowires Reveals Stacked Hemes that Transport Electrons over Micrometers. *Cell* **2019**, *177*, 361−369 e10.
(63) Wang, F. A.-O. X.; Chan, C. H.; Suciu, V.; Mustafa, K.; Ammend, M.; Si, D.; Hochbaum, A. I.; Egelman, E. H.; Bond, D. R. Structure of Geobacter OmcZ filaments suggests extracellular cytochrome polymers evolved independently multiple times. *eLife* **2022**, *11*, No. e81551.
(64) Hansen, J.-P.; McDonald, I. R. *Theory of Simple Liquids*, 4th ed.; Academic Press, 2013.
(65) Matyushov, D. V. Energetics of Electron-Transfer Reactions in Soft Condensed Media. *Acc. Chem. Res.* **2007**, *38*, 294−301.
(66) Phillips, J. C.; Hardy, D. J.; Maia, J. D. C.; Stone, J. E.; Ribeiro, J. V.; Bernardi, R. C.; Buch, R.; Fiorin, G.; Hénin, J.; Jiang, W.; McGreevy, R.; Melo, M. C. R.; Radak, B. K.; Skeel, R. D.; Singharoy, A.; Wang, Y.; Roux, B.; Aksimentiev, A.; Luthey-Schulten, Z.; Kalé, L. V.; Schulten, K.; Chipot, C.; Tajkhorshid, E. Scalable molecular dynamics on CPU and GPU architectures with NAMD. *J. Chem. Phys.* **2020**, *153*, 044130.
(67) Huang, J.; Rauscher, S.; Nawrocki, G.; Ran, T.; Feig, M.; de Groot, B. L.; Grubmüller, H.; MacKerell, A. D. CHARMM36m: an improved force field for folded and intrinsically disordered proteins. *Nat. Methods* **2017**, *14*, 71−73.
(68) Jorgensen, W. L.; Chandrasekhar, J.; Madura, J. D.; Impey, R. W.; Klein, M. L. Comparison of simple potential functions for simulating liquid water. *J. Chem. Phys.* **1983**, *79*, 926−935.
(69) Nosé, S.; Klein, M. L. Constant pressure molecular dynamics for molecular systems. *Mol. Phys.* **1983**, *50*, 1055−1076.
(70) Feller, S. E.; Zhang, Y.; Pastor, R. W.; Brooks, B. R. Constant pressure molecular dynamics simulation: The Langevin piston method. *J. Chem. Phys.* **1995**, *103*, 4613−4621.
(71) Kajander, T.; Cortajarena, A. L.; Mochrie, S.; Regan, L. Structure and stability of designed TPR protein superhelices: unusual crystal packing and implications for natural TPR proteins. *Acta Crystallogr., Sect. D: Biol. Crystallogr.* **2007**, *63*, 800−811.
(72) Zhang, Y. I-TASSER server for protein 3D structure prediction. *BMC Bioinf.* **2008**, *9*, 40.
(73) Jorgensen, W. L.; Chandrasekhar, J.; Madura, J. D.; Impey, R. W.; Klein, M. L. Comparison of simple potential functions for simulating liquid water. *J. Chem. Phys.* **1983**, *79*, 926−935.

https://doi.org/10.1021/acsphyschemau.3c00017
ACS Phys. Chem Au 2023, 3, 444−455